Supplementary Note 1. Physical system

N ^{88}Sr atoms are confined in a one-dimensional (1D) optical lattice (wavelength $\lambda_{\mathrm{L}} = 813$ nm) formed inside a hollow-core photonic crystal fibre (HCPCF) along the axial direction (in the z-axis). The quantum axis is set by an external magnetic field $\mathbf{B}_0 = (0.14\ \mathrm{mT})\hat{\mathbf{e}}_x$. Here, $\hat{\mathbf{e}}_x$ is the unit vector in the direction of the x-axis. The in-fibre atoms are coupled with the superradiant (SR) field

$$\mathbf{E}_{\mathrm{SR}}(\mathbf{r}, z; t) = (\hat{\mathbf{e}}_x/2)E_{\mathrm{SR}}(\mathbf{r}, z; t)e^{-i\omega_0 t} + (\hat{\mathbf{e}}_x/2)E^*_{\mathrm{SR}}(\mathbf{r}, z; t)e^{i\omega_0 t}, \tag{S1}$$

via the $^1S_0 - {}^3P_1(m = 0)$ intercombination transition (frequency $\omega_0 = 2\pi \times 435$ THz, wavelength $\lambda_0 = 2\pi c/\omega_0$ in vacuum, and spontaneous decay rate $\gamma_0 = 2\pi \times 7.5$ kHz). c is the speed of light in vacuum. $\mathbf{r} = x\hat{\mathbf{e}}_x + y\hat{\mathbf{e}}_y$ is the radial coordinate and $\hat{\mathbf{e}}_y$ is the unit vector in the direction of the y-axis. $E_{\mathrm{SR}}(\mathbf{r}, z; t)$ denotes the complex amplitude of SR field. The linear-polarization vector of the optical lattice lasers is chosen to fulfil the magic condition[1] which cancels the light-shift difference between $^1S_0$ and $^3P_1(m = 0)$. The symbol (u, μ) is used to label the μ-th atom in the u-th lattice site.

The characteristic length of the in-fibre confined atomic cloud along the axial direction is l_z. In the main text, we only focus on two specific values, i.e., $l_z = 0.87$ mm for the unexpanded cloud and $l_z = 2.1$ mm for the expanded cloud. The corresponding lattice-site numbers N_{L} are then given by $N_{\mathrm{L}} = l_z/(\lambda_{\mathrm{L}}/2) = 2.1 \times 10^3$ (unexpanded) and $N_{\mathrm{L}} = 5.2 \times 10^3$ (expanded). Assuming a Gaussian atomic distribution over the optical-lattice region, the number of atoms in the u-th lattice site reaches

$$N_u = \left[N\lambda_{\mathrm{L}}/\left(\sqrt{\pi}l_z\right)\right] \exp[-(\tilde{z}_u - \tilde{z}_{\mathrm{c}})^2/(l_z/2)^2], \tag{S2}$$

where $\tilde{z}_u$ denotes the central position of the u-th lattice site in the axial direction and $\tilde{z}_{\mathrm{c}}$ is the central position of the atomic cloud along the axial direction. Summing N_u over all lattice sites results in the total number of atoms, i.e., $N = \sum_{u=1}^{N_{\mathrm{L}}} N_u$. In the u-th lattice site, N_u atoms spread within a pancake-shaped potential with the characteristic axial (z-axis) width $l_{\mathrm{a}} = 54$ nm and radial ($x - y$ plane) radius $r_{\mathrm{a}} = 1.7$ μm and follow the Gaussian distributions

$$[1/(\pi r_{\mathrm{a}}^2)] \exp\left[-\left|\mathbf{r}_{(u,\mu)}\right|^2/r_{\mathrm{a}}^2\right] \quad \text{and} \quad \left[2/\left(\sqrt{\pi}l_{\mathrm{a}}\right)\right] \exp\left[-\left|z_{(u,\mu)} - \tilde{z}_u\right|^2/(l_{\mathrm{a}}/2)^2\right], \tag{S3}$$

in the radial plane and the axial direction, respectively. Here $\mathbf{r}_{(u,\mu)} + z_{(u,\mu)}\hat{\mathbf{e}}_z$ corresponds to the spatial position of the (u, μ)-th atom. $\hat{\mathbf{e}}_z$ is the unit vector in the direction of the z-axis.

For the atoms in the same lattice site, the interatomic distance may be shorter than λ_0, leading to the virtual-photon-mediated resonant dipole-dipole interaction[2]. In contrast, the interaction between two atoms in different lattice sites is weak and negligible because of $(\lambda_{\mathrm{L}}/2) > (\lambda_0/2\pi)$.

Supplementary Note 2. Equations of motion for atoms

The Hamiltonian describing the coherent atom-light interface and long-range dipolar interaction is written as[2]

$$\begin{aligned}\hat{H} = &\sum_u \sum_{\mu}^{(u)} \hbar\omega_0 \hat{\sigma}_{(u,\mu)}^{\dagger}\hat{\sigma}_{(u,\mu)} + \hbar\gamma_0 \sum_u \sum_{\mu_1}^{(u)} \sum_{\mu_2\neq\mu_1}^{(u)} G_{u,(\mu_1\mu_2)} \hat{\sigma}_{(u,\mu_1)}^{\dagger}\hat{\sigma}_{(u,\mu_2)} \\ &+ \sum_u \sum_{\mu}^{(u)} \left[-\frac{1}{2} D E_{\mathrm{SR}}\left(\mathbf{r}_{(u,\mu)}, z_{(u,\mu)}; t\right)\hat{\sigma}_{(u,\mu)}^{\dagger} e^{-i\omega_0 t} + \mathrm{h.c.}\right], \end{aligned} \tag{S4}$$

where the operator associated with the (u,μ)-th atom is defined as $\hat{\sigma}_{(u,\mu)} = \left(\left|\,^1S_0\right\rangle\left\langle\,^3P_1(m=0)\right|\right)_{(u,\mu)}$, the dipole moment is $D = (3\pi\hbar\varepsilon_0 c^3\gamma_0/\omega_0^3)^{1/2}$, and the symbol $\sum_{\mu}^{(u)}$ ... denotes the summation over the atoms in the u-th lattice site. $\hbar$ is the reduced Planck's constant and ε_0 is the vacuum permittivity. $E_{\mathrm{SR}}\left(\mathbf{r}_{(u,\mu)}, z_{(u,\mu)}; t\right)$ is the SR-field amplitude at the (u,μ)-th atomic position. The parameter

$$\begin{aligned} G_{u,(\mu_1\mu_2)} = \frac{3}{4}\Bigg[&-\left(1-\cos^2\theta_{u,(\mu_1\mu_2)}\right)\frac{\cos\beta_{u,(\mu_1\mu_2)}}{\beta_{u,(\mu_1\mu_2)}} \\ &+\left(1-3\cos^2\theta_{u,(\mu_1\mu_2)}\right)\left(\frac{\sin\beta_{u,(\mu_1\mu_2)}}{\beta_{u,(\mu_1\mu_2)}^2}+\frac{\cos\beta_{u,(\mu_1\mu_2)}}{\beta_{u,(\mu_1\mu_2)}^3}\right)\Bigg], \end{aligned} \tag{S5}$$

characterizes the coherent virtual-photon-mediated dipolar interaction between two atoms (u,μ_1) and (u,μ_2) in the μ-th lattice site. The normalized interatomic distance is given by $\beta_{u,(\mu_1\mu_2)} = 2\pi\left|\mathbf{r}_{(u,\mu_1)} - \mathbf{r}_{(u,\mu_2)}\right|/\lambda_0$ and the angle between the light-induced-dipole vector (along $\hat{\mathbf{e}}_x$) and the $\left(\mathbf{r}_{(u,\mu_1)} - \mathbf{r}_{(u,\mu_2)}\right)$ vector is $\theta_{u,(\mu_1\mu_2)}$. For $\beta_{u,(\mu_1\mu_2)} < 1$, the $\sim\beta_{u,(\mu_1\mu_2)}^{-3}$ term plays the predominant role, i.e., $G_{u,(\mu_1\mu_2)} \propto \beta_{u,(\mu_1\mu_2)}^{-3}$. The Heisenberg equation for an arbitrary atomic operator $\hat{O}$ is then expressed as

$$\begin{aligned}\frac{d}{dt}\hat{O} = &\sum_u \sum_{\mu_1}^{(u)} \left(i\omega_0\left[\hat{\sigma}_{(u,\mu_1)}^{\dagger}\hat{\sigma}_{(u,\mu_1)}, \hat{O}\right] + i\gamma_0 \sum_{\mu_2\neq\mu_1}^{(u)} G_{u,(\mu_1\mu_2)}\left[\hat{\sigma}_{(u,\mu_1)}^{\dagger}\hat{\sigma}_{(u,\mu_2)}, \hat{O}\right]\right) \\ &+ \sum_u \sum_{\mu}^{(u)} \left(-i\frac{D}{2\hbar} E_{\mathrm{SR}}\left(\mathbf{r}_{(u,\mu)}, z_{(u,\mu)}; t\right)\left[\hat{\sigma}_{(u,\mu)}^{\dagger}, \hat{O}\right] e^{-i\omega_0 t} + \mathrm{h.c.}\right) \\ &+\gamma_0 \sum_u \sum_{\mu_1}^{(u)} \sum_{\mu_2}^{(u)} R_{u,(\mu_1\mu_2)}\left(\hat{\sigma}_{(u,\mu_1)}^{\dagger}\hat{O}\hat{\sigma}_{(u,\mu_2)}\right.\end{aligned}$$

$$-\frac{1}{2}\hat{\sigma}^{\dagger}_{(u,\mu_1)}\hat{\sigma}_{(u,\mu_2)}\hat{O}-\frac{1}{2}\hat{O}\hat{\sigma}^{\dagger}_{(u,\mu_1)}\hat{\sigma}_{(u,\mu_2)}\Big), \tag{S6}$$

where we have taken into account the dissipative dipolar interatomic coupling characterized by the parameter[2]

$$R_{u,(\mu_1\mu_2)}=\frac{3}{2}\Big[\big(1-\cos^2\theta_{u,(\mu_1\mu_2)}\big)\frac{\sin\beta_{u,(\mu_1\mu_2)}}{\beta_{u,(\mu_1\mu_2)}} +\big(1-3\cos^2\theta_{u,(\mu_1\mu_2)}\big)\Big(\frac{\cos\beta_{u,(\mu_1\mu_2)}}{\beta^2_{u,(\mu_1\mu_2)}}-\frac{\sin\beta_{u,(\mu_1\mu_2)}}{\beta^3_{u,(\mu_1\mu_2)}}\Big)\Big], \tag{S7}$$

For $\mathbf{r}_{(u,\mu_1)}=\mathbf{r}_{(u,\mu_2)}$, we have $R_{u,(\mu_1\mu_2)}=1$.

Based on Supplementary eq. S6, one can derive the Heisenberg equations for the lowering $\hat{\sigma}_{(u,\mu)}$ and population-difference $\hat{w}_{(u,\mu)}=\hat{\sigma}^{\dagger}_{(u,\mu)}\hat{\sigma}_{(u,\mu)}-\hat{\sigma}_{(u,\mu)}\hat{\sigma}^{\dagger}_{(u,\mu)}$ operators, i.e.,

$$\frac{d}{dt}\hat{\sigma}_{(u,\mu_1)}=\Big(-\frac{\gamma_0}{2}-i\omega_0\Big)\hat{\sigma}_{(u,\mu_1)}+\Big[-i\frac{D}{2\hbar}E_{\mathrm{SR}}\big(\mathbf{r}_{(u,\mu_1)},z_{(u,\mu_1)};t\big)e^{-i\omega_0 t} +\gamma_0\sum\nolimits^{(u)}_{\mu_2\neq\mu_1}\Big(\frac{R_{u,(\mu_1\mu_2)}}{2}+iG_{u,(\mu_1\mu_2)}\Big)\hat{\sigma}_{(u,\mu_2)}\Big]\hat{w}_{(u,\mu_1)}, \tag{S8a}$$

$$\begin{aligned}\frac{d}{dt}\hat{w}_{(u,\mu_1)}=&-\gamma_0\big(\hat{w}_{(u,\mu_1)}+1\big)-2\hat{\sigma}^{\dagger}_{(u,\mu_1)}\Big[-i\frac{D}{2\hbar}E_{\mathrm{SR}}\big(\mathbf{r}_{(u,\mu_1)},z_{(u,\mu_1)};t\big)e^{-i\omega_0 t}\\ &+\gamma_0\sum\nolimits^{(u)}_{\mu_2\neq\mu_1}\Big(\frac{R_{u,(\mu_1\mu_2)}}{2}+iG_{u,(\mu_1\mu_2)}\Big)\hat{\sigma}_{(u,\mu_2)}\Big]\\ &-2\Big[i\frac{D}{2\hbar}E^{*}_{\mathrm{SR}}\big(\mathbf{r}_{(u,\mu_1)},z_{(u,\mu_1)};t\big)e^{i\omega_0 t}\\ &+\gamma_0\sum\nolimits^{(u)}_{\mu_2\neq\mu_1}\Big(\frac{R_{u,(\mu_1\mu_2)}}{2}-iG_{u,(\mu_1\mu_2)}\Big)\hat{\sigma}^{\dagger}_{(u,\mu_2)}\Big]\hat{\sigma}_{(u,\mu_1)},\end{aligned} \tag{S8b}$$

Defining $\hat{\tilde{\sigma}}_{(u,\mu)}=\hat{\sigma}_{(u,\mu)}e^{i\omega_0 t}$ and taking the quantum average, e.g., $\langle\hat{\tilde{\sigma}}_{(u,\mu)}\rangle$ and $\langle\hat{w}_{(u,\mu)}\rangle$, we arrive at

$$\frac{d}{dt}\langle\hat{\tilde{\sigma}}_{(u,\mu_1)}\rangle=-\frac{\gamma_0}{2}\langle\hat{\tilde{\sigma}}_{(u,\mu_1)}\rangle-i\frac{D}{2\hbar}E_{\mathrm{SR}}\big(\mathbf{r}_{(u,\mu_1)},z_{(u,\mu_1)};t\big)\langle\hat{w}_{(u,\mu_1)}\rangle +\gamma_0\sum\nolimits^{(u)}_{\mu_2\neq\mu_1}\Big(\frac{R_{u,(\mu_1\mu_2)}}{2}+iG_{u,(\mu_1\mu_2)}\Big)\langle\hat{\tilde{\sigma}}_{(u,\mu_2)}\hat{w}_{(u,\mu_1)}\rangle, \tag{S9a}$$

$$\begin{aligned}\frac{d}{dt}\langle\hat{w}_{(u,\mu_1)}\rangle=&-\gamma_0\big(\langle\hat{w}_{(u,\mu_1)}\rangle+1\big)+2i\frac{D}{2\hbar}\Big[E_{\mathrm{SR}}\big(\mathbf{r}_{(u,\mu_1)},z_{(u,\mu_1)};t\big)\langle\hat{\tilde{\sigma}}^{\dagger}_{(u,\mu_1)}\rangle\\ &-E^{*}_{\mathrm{SR}}\big(\mathbf{r}_{(u,\mu_1)},z_{(u,\mu_1)};t\big)\langle\hat{\tilde{\sigma}}_{(u,\mu_1)}\rangle\Big]\\ &-2\gamma_0\sum\nolimits^{(u)}_{\mu_2\neq\mu_1}\Big[\Big(\frac{R_{u,(\mu_1\mu_2)}}{2}+iG_{u,(\mu_1\mu_2)}\Big)\langle\hat{\tilde{\sigma}}^{\dagger}_{(u,\mu_1)}\hat{\tilde{\sigma}}_{(u,\mu_2)}\rangle\\ &+\Big(\frac{R_{u,(\mu_1\mu_2)}}{2}-iG_{u,(\mu_1\mu_2)}\Big)\langle\hat{\tilde{\sigma}}^{\dagger}_{(u,\mu_2)}\hat{\tilde{\sigma}}_{(u,\mu_1)}\rangle\Big].\end{aligned} \tag{S9b}$$

We further apply the zero-order approximation, for example,

$$\langle\hat{\tilde{\sigma}}_{(u,\mu_1)}(t)\hat{w}_{(u,\mu_2\neq\mu_1)}(t)\rangle\approx\langle\hat{\tilde{\sigma}}_{(u,\mu_1)}(t)\rangle\langle\hat{w}_{(u,\mu_2\neq\mu_1)}(t)\rangle,$$

to simplify the mathematical model. The validity of this approximation can be confirmed by comparing the computed SR behavior and the experimental results (see below and main text). The symbols $s_{(u,\mu)}(t)$ and $w_{(u,\mu)}(t)$ are used to respectively replace $\langle\hat{\tilde{\sigma}}_{(u,\mu)}(t)\rangle$ and $\langle\hat{w}_{(u,\mu)}(t)\rangle$. Finally, we obtain the equations of motion for the atoms

$$\frac{d}{dt}s_{(u,\mu_1)} = -\frac{\gamma_0}{2}s_{(u,\mu_1)} - i\left[\frac{D}{2\hbar}E_{\mathrm{SR}}\left(\mathbf{r}_{(u,\mu_1)},\tilde{z}_u;t\right)\right.$$
$$\left.+i\gamma_0\sum_{\mu_2\neq\mu_1}^{(u)}\left(\frac{R_{u,(\mu_1\mu_2)}}{2}+iG_{u,(\mu_1\mu_2)}\right)s_{(u,\mu_2)}\right]w_{(u,\mu_1)}, \quad \text{(S10a)}$$

$$\frac{d}{dt}w_{(u,\mu_1)} = -\gamma_0\left(w_{(u,\mu_1)}+1\right) + 2i\left[\frac{D}{2\hbar}E_{\mathrm{SR}}\left(\mathbf{r}_{(u,\mu_1)},\tilde{z}_u;t\right)\right.$$
$$\left.+i\gamma_0\sum_{\mu_2\neq\mu_1}^{(u)}\left(\frac{R_{u,(\mu_1\mu_2)}}{2}+iG_{u,(\mu_1\mu_2)}\right)s_{(u,\mu_2)}\right]s^*_{(u,\mu_1)}$$
$$-2i\left[\frac{D}{2\hbar}E^*_{\mathrm{SR}}\left(\mathbf{r}_{(u,\mu_1)},\tilde{z}_u;t\right)\right.$$
$$\left.-i\gamma_0\sum_{\mu_2\neq\mu_1}^{(u)}\left(\frac{R_{u,(\mu_1\mu_2)}}{2}-iG_{u,(\mu_1\mu_2)}\right)s^*_{(u,\mu_2)}\right]s_{(u,\mu_1)}, \quad \text{(S10b)}$$

where we have approximated the amplitude $E_{\mathrm{SR}}\left(\mathbf{r}_{(u,\mu)},z_{(u,\mu)};t\right)$ at the (u,μ)-th atomic position by the value $E_{\mathrm{SR}}\left(\mathbf{r}_{(u,\mu)},\tilde{z}_u;t\right)$ at the central position of the u-th lattice site, i.e., we have assumed that $E_{\mathrm{SR}}\left(\mathbf{r}_{(u,\mu)},z_{(u,\mu)};t\right)$ does not vary apparently within the length scale of l_{a}.

Supplementary Note 3. Equation of motion for SR field

We now derive the equation of motion for the light field inside the fibre. Applying Maxwell's equations, one has

$$(\partial_{\mathbf{r}}^2 - c^{-2}\partial_t^2 + \partial_z^2)\mathbf{E}_{\mathrm{SR}}(\mathbf{r},z;t) = \mu_0\partial_t^2\mathbf{P}(\mathbf{r},z;t). \quad \text{(S11)}$$

μ_0 is the vacuum permeability. The medium polarizability is given by

$$\mathbf{P}(\mathbf{r},z;t) = (\hat{\mathbf{e}}_x/2)\chi_{\mathrm{e}}(\mathbf{r})\varepsilon_0 E_{\mathrm{SR}}(\mathbf{r},z;t)e^{-i\omega_0 t}$$
$$+\hat{\mathbf{e}}_x D\sum_u\sum_\mu^{(u)}\langle\hat{\sigma}_{(u,\mu)}(t)\rangle\delta\left(\mathbf{r}-\mathbf{r}_{(u,\mu)}\right)\delta\left(z-z_{(u,\mu)}\right) + \text{c. c.}, \quad \text{(S12)}$$

where $\chi_{\mathrm{e}}(\mathbf{r})$ is the electric susceptibility of the fibre in the absence of lattice-confined atoms. Substituting above expression into Supplementary eq. S11, we are left with

$$[\partial_{\mathbf{r}}^2 - c^{-2}n^2(\mathbf{r})\partial_t^2 + \partial_z^2]E_{\mathrm{SR}}(\mathbf{r},z;t)e^{-i\omega_0 t}$$
$$= 2\mu_0 D\partial_t^2\sum_u\sum_\mu^{(u)}\langle\hat{\tilde{\sigma}}_{(u,\mu)}(t)\rangle e^{-i\omega_0 t}\delta\left(\mathbf{r}-\mathbf{r}_{(u,\mu)}\right)\delta\left(z-z_{(u,\mu)}\right). \quad \text{(S13)}$$

Here $n(\mathbf{r}) = \sqrt{1+\chi_e(\mathbf{r})}$ denotes the refractive-index profile of the fibre's cross-section.

In the absence of atoms, one obtains a time-independent equation from (S13),

$$[\partial_{\mathbf{r}}^2 + n^2(\mathbf{r})\omega_0^2/c^2 + \partial_z^2]E(\mathbf{r},z) = 0, \tag{S14}$$

for a general in-fibre light amplitude $E(\mathbf{r},z)$. Following the separation of variables procedure, Supplementary eq. S14 leads to the m-th transverse eigenmode $\psi_m(\mathbf{r})$ with the corresponding effective refractive index n_m^{eff}, i.e.,

$$[\partial_{\mathbf{r}}^2 + n^2(\mathbf{r})\omega_0^2/c^2]\psi_m(\mathbf{r})e^{in_m^{\text{eff}}\omega_0 z/c} = \left(n_m^{\text{eff}}\omega_0/c\right)^2\psi_m(\mathbf{r})e^{in_m^{\text{eff}}\omega_0 z/c}, \tag{S15a}$$

$$\partial_z^2\psi_m(\mathbf{r})e^{in_m^{\text{eff}}\omega_0 z/c} = -\left(n_m^{\text{eff}}\omega_0/c\right)^2\psi_m(\mathbf{r})e^{in_m^{\text{eff}}\omega_0 z/c}. \tag{S15b}$$

The normalization condition is given by $\iint \psi_m^*(\mathbf{r})\psi_{m'}(\mathbf{r})d^2\mathbf{r} = \delta_{m,m'}$. $\psi_0(\mathbf{r})$ corresponds to the Gaussian-like fundamental HE_{11} mode. Based on $\psi_m(\mathbf{r})$, the SR amplitude $E_{\text{SR}}(\mathbf{r},z;t)$ may be rewritten in a superposition form

$$E_{\text{SR}}(\mathbf{r},z;t) = \sum_m f_m(z,t)\psi_m(\mathbf{r})e^{in_m^{\text{eff}}\omega_0 z/c}. \tag{S16}$$

$|f_m(z,t)|^2$ correspond to the mode weights. Substituting Supplementary eq. S16 into Supplementary eq. S13 and using the slowly varying envelope approximation, $|\partial_t f_m(z,t)| \ll \omega_0|f_m(z,t)|$ and $|\partial_z f_m(z,t)| \ll \left(n_m^{\text{eff}}\omega_0/c\right)|f_m(z,t)|$, we arrive at

$$\begin{aligned}&\sum_m\left(n_m^{\text{eff}}+1\right)[(\partial_z + c^{-1}\partial_t)f_m(z,t)]\psi_m(\mathbf{r})e^{in_m^{\text{eff}}\omega_0 z/c}\\ &\qquad = i\tfrac{2D\omega_0}{\varepsilon_0 c}\sum_u\sum_\mu^{(u)}\langle\hat{\tilde{\sigma}}_{(u,\mu)}(t)\rangle\delta\left(\mathbf{r}-\mathbf{r}_{(u,\mu)}\right)\delta\left(z-z_{(u,\mu)}\right),\end{aligned} \tag{S17}$$

which further leads to

$$\begin{aligned}&(\partial_z + c^{-1}\partial_t)f_m(z,t)\\ &\quad = i\tfrac{2D\omega_0}{\varepsilon_0 c\left(n_m^{\text{eff}}+1\right)}\sum_u\sum_\mu^{(u)}\langle\hat{\tilde{\sigma}}_{(u,\mu)}(t)\rangle\psi_m^*\left(\mathbf{r}_{(u,\mu)}\right)e^{-in_m^{\text{eff}}\omega_0 z_{(u,\mu)}/c}\delta\left(z-z_{(u,\mu)}\right).\end{aligned} \tag{S18}$$

We integrate Supplementary eq. S18 around the central position $\tilde{z}_u$ of the u-th lattice site within the range of $\tilde{z}_u - \lambda_{\text{L}}/4 < z < \tilde{z}_u + \lambda_{\text{L}}/4$,

$$\begin{aligned}\int_{\tilde{z}_u-\lambda_{\text{L}}/4}^{\tilde{z}_u+\lambda_{\text{L}}/4}(\partial_z + c^{-1}\partial_t)f_m(z,t)dz &= f_m(\tilde{z}_u+\lambda_{\text{L}}/4\,,t) - f_m(\tilde{z}_u-\lambda_{\text{L}}/4\,,t)\\ &\quad + c^{-1}\partial_t\int_{\tilde{z}_u-\lambda_{\text{L}}/4}^{\tilde{z}_u+\lambda_{\text{L}}/4} f_m(z,t)dz.\end{aligned} \tag{S19}$$

and obtain

$$\begin{aligned}f_m(\tilde{z}_u+\lambda_{\text{L}}/4\,,t) &= f_m(\tilde{z}_u-\lambda_{\text{L}}/4\,,t)\\ &\quad + i\tfrac{2D\omega_0}{\varepsilon_0 c\left(n_m^{\text{eff}}+1\right)}\sum_\mu^{(u)} s_{(u,\mu)}(t)\psi_m^*\left(\mathbf{r}_{(u,\mu)}\right)e^{-in_m^{\text{eff}}\omega_0 z_{(u,\mu)}/c}.\end{aligned} \tag{S20}$$

In deriving Supplementary eq. S20 we have substituted $s_{(u,\mu)}(t)$ for $\langle\hat{\tilde{\sigma}}_{(u,\mu)}(t)\rangle$ and omitted the term $c^{-1}\partial_t\int_{\tilde{z}_u-\lambda_{\text{L}}/4}^{\tilde{z}_u+\lambda_{\text{L}}/4} f_m(z,t)dz$ in Supplementary eq. S19 since its effect is negligible in the

slowly varying envelope approximation. Further, the $e^{-in_m^{\mathrm{eff}}\omega_0 z_{(u,\mu)}/c}$ term in Supplementary eq. S20 may be approximated as $e^{-in_m^{\mathrm{eff}}\omega_0 \tilde{z}_u/c}$ due to the fact $\omega_0 l_\mathrm{a}/c \ll 1$. Defining $\tilde{f}_{u,m}(t) = f_m(\tilde{z}_u - \lambda_\mathrm{L}/4\,, t)e^{in_m^{\mathrm{eff}}\omega_0(\tilde{z}_u-\lambda_\mathrm{L}/4)/c}$, one has

$$\tilde{f}_{u+1,m}(t)e^{-in_m^{\mathrm{eff}}\omega_0(\lambda_\mathrm{L}/4)/c} = \tilde{f}_{u,m}(t)e^{in_m^{\mathrm{eff}}\omega_0(\lambda_\mathrm{L}/4)/c} + i\frac{2D\omega_0}{\varepsilon_0 c(n_m^{\mathrm{eff}}+1)}\sum_\mu^{(u)} s_{(u,\mu)}(t)\psi_m^*(\mathbf{r}_{(u,\mu)}), \quad \text{(S21)}$$

where we have used the relation $\tilde{z}_{u+1} - \tilde{z}_u = \lambda_\mathrm{L}/2$. From Supplementary eq. S21 one may solve the time-evolved SR amplitude $E_\mathrm{SR}(\mathbf{r}, \tilde{z}_u - \lambda_\mathrm{L}/4\,; t) = \sum_m \tilde{f}_{u,m}(t)\psi_m(\mathbf{r})$ at the spot of $[\mathbf{r} + (\tilde{z}_u - \lambda_\mathrm{L}/4)\hat{\mathbf{e}}_z]$.

$E_\mathrm{SR}(\mathbf{r}, \tilde{z}_{u=1} - \lambda_\mathrm{L}/4\,; t)$ ($u = 1$ denotes the first lattice site) is determined by the input pump-field amplitude $E_\mathrm{p}(\mathbf{r}, t)$ which is linearly polarized in the x-direction. In experiment, $E_\mathrm{p}(\mathbf{r}, t)$ is a π-pulse with a duration $\tau_\mathrm{p} = 500$ ns. Applying the slowly varying envelope approximation, the SR amplitude at the central position of the u-th lattice site may be approximated as $E_\mathrm{SR}(\mathbf{r}, \tilde{z}_u; t) = \sum_m \tilde{f}_{u,m}^{(1/2)}\psi_m(\mathbf{r})e^{in_m^{\mathrm{eff}}\omega_0\tilde{z}_u/c}$ with

$$2\tilde{f}_{u,m}^{(1/2)} = \tilde{f}_{u,m}(t)e^{in_m^{\mathrm{eff}}\omega_0(\lambda_\mathrm{L}/4)/c} + \tilde{f}_{u+1,m}(t)e^{-in_m^{\mathrm{eff}}\omega_0(\lambda_\mathrm{L}/4)/c}. \quad \text{(S22)}$$

$E_\mathrm{SR}\left(\mathbf{r}, \tilde{z}_{u=N_\mathrm{L}+1} - \lambda_\mathrm{L}/4\,; t\right)$ corresponds to the SR field output from the fibre. For simplicity, in the following we use the symbol $E_\mathrm{SR}(\mathbf{r}, t)$ to denote the amplitude of the output SR.

Supplementary Note 4. Multiple transverse modes

The HCPCF used in experiment supports multimode propagation. For the convenience here we apply the scalar wave approximation to the linearly polarized mode classification, $\mathrm{LP}_{l,\mu}$. l and μ are the indices corresponding to the azimuthal and radial field variation, respectively. Thus, the HE_{11} mode is labelled as LP_{01}. The fibre guides via Inhibited Coupling mechanism[3]. Consequently, its modes are leaky and suffer of confinement loss. Confinement loss coefficient quantifies the fraction of power lost by the mode due to the leakage in the fibre cladding per unit of length. Supplementary Figure 1 lists the numerically simulated (using a full-vector finite element method[3]) mode intensity profiles of the first nine lowest-loss guided modes of the HCPCF along with their respective effective refractive indices $n_{m=0,1,\ldots,8}^{\mathrm{eff}}$ and confinement loss coefficients $\alpha_{m=0,1,\ldots,8}$. The results show that the LP_{01} mode has the lowest confinement loss of ~0.01 dB m^{-1} at 813 nm while the LP_{02} mode suffers the highest loss of 4 dB m^{-1}. The fundamental LP_{01} mode has a beam radius

$w_0 = 11.8$ μm, showing a good matching with the pump field, i.e., $E_{\mathrm{p}}(\mathbf{r},t) \propto \psi_0(\mathbf{r})e^{-i\Delta_{\mathrm{p}}t}$ ($\Delta_{\mathrm{p}} = \omega_{\mathrm{p}} - \omega_0$ is the detuning and ω_{p} is the pump-field frequency).

To keep our computation load to a reasonable level for solving our equations of motion, we limit the number of transverse modes to a maximum of 9, i.e., to the ones shown in Supplementary Fig. 1. It is noteworthy that when choosing the most dominant modes in the SR dynamics, both the loss of the fibre modes and their coupling strength with the atomic cloud have been taken into account: (i) Indeed, for the fibre modes with the comparable confinement losses, the modes, whose intensity distributions show a maximum at the centre of the fibre cross section (i.e., $\mathrm{LP}_{0,\mu}$), have the stronger coupling strength with the atomic cloud than those whose intensity distributions have a zero at the centre of the fibre core (i.e., $\mathrm{LP}_{l,\mu}$ with $l > 0$); and (ii) The confinement loss increases with high orders l and μ. Consequently, the atoms hardly interact with the modes, whose intensity distributions peak at the central point of the fibre core but have the peak diameters smaller than $2r_{\mathrm{a}}$ *or* do not have central peaks at all.

Supplementary Note 5. Numerical simulation

The time evolution of the whole system can be numerically simulated based on Supplementary eq. S10a, S10b and S21 via the fourth-order Runge-Kutta technique. The spatial positions of N atoms are randomly generated according to $\left[(N\lambda_{\mathrm{L}})/\left(\sqrt{\pi}l_z\right)\right]e^{-(\tilde{z}_u-\tilde{z}_{\mathrm{c}})^2/(l_z/2)^2}$ and the Gaussian distributions of $(\pi r_{\mathrm{a}}^2)^{-1}\exp\left[-\left|\boldsymbol{r}_{(u,\mu)}\right|^2/r_{\mathrm{a}}^2\right]$ in the radial plane and $\left[2/\left(\sqrt{\pi}l_{\mathrm{a}}\right)\right]\exp\left[-\left|z_{(u,\mu)}-\tilde{z}_u\right|^2/(l_{\mathrm{a}}/2)^2\right]$ in the axial direction (see Supplementary Fig. 2a and 2b). For the u-th lattice site, the average on-site atomic density is

$$\rho_u = N_u/(\pi r_{\mathrm{a}}^2 l_{\mathrm{a}}) = \rho\left(2/\sqrt{\pi}\right)\exp[-(\tilde{z}_u-\tilde{z}_{\mathrm{c}})^2/(l_z/2)^2], \tag{S23}$$

where we have defined the atomic density $\rho = N_{\mathrm{a}}/(\pi r_{\mathrm{a}}^2 l_{\mathrm{a}})$ averaged over the whole lattice region with the averaged on-site atomic number $N_{\mathrm{a}} = N/N_{\mathrm{L}}$.

Our numerical simulation well reproduces the ringing behaviour observed in experiment. The raw heterodyne signal $\tilde{V}_{\mathrm{cal}}(t)$ described in Fig. 5a of the main text is given by $\tilde{V}_{\mathrm{cal}}(t) \propto \mathrm{Re}\left[e^{-i\Omega_0 t}\iint E_{\mathrm{LO}}(\mathbf{r})E_{\mathrm{SR}}^{'}(\mathbf{r},t)d^2\mathbf{r}\right]$, where Re[...] is the real part and $\Omega_0 = \omega_0 - \omega_{\mathrm{LO}}$. $E_{\mathrm{LO}}(\mathbf{r})$ and ω_{LO} are the amplitude and frequency of the local optical oscillator. The amplitude $E_{\mathrm{SR}}^{'}(\mathbf{r},t)$ corresponds to the SR field propagating in the single-mode fibre (shown in Fig. 1c of the main

text) and is given by $E_{\mathrm{SR}}^{'}(\mathbf{r},t) = [\iint \phi_0^*(\mathbf{r}) E_{\mathrm{SR}}(\mathbf{r},t) d^2\mathbf{r}]\phi_0(\mathbf{r})$. Here $\phi_0(\mathbf{r}) = \sqrt{2/(\pi\widetilde{w}_0^2)}\, e^{-|\mathbf{r}|^2/\widetilde{w}_0^2}$ is the Gaussian-like ground mode of the single-mode fibre with the beam radius of $\widetilde{w}_0 = 0.4w_0$. The band-pass filter removes the unwanted rapid varying component in $\tilde{V}_{\mathrm{cal}}(t)$, leading to the amplitude $V_{\mathrm{cal}}(t)$. Figure 5a of the main text shows the numerical result $V_{\mathrm{cal}}(t)$ that corresponds to the experimental result $V_{\mathrm{RF}}(t)$ shown in Fig. 2a of the main text. It is seen that the theoretical result is consistent with the experimental measurement, proving the validity of the approximation $\langle \hat{\tilde{\sigma}}_{(u,\mu_1)}(t)\hat{w}_{(u,\mu_2\neq\mu_1)}(t)\rangle \approx \langle \hat{\tilde{\sigma}}_{(u,\mu_1)}(t)\rangle\langle \hat{w}_{(u,\mu_2\neq\mu_1)}(t)\rangle$, i.e., the effect of quantum correlation on the SR behavior is negligible. Supplementary Movie 1 also displays an example time evolution of SR for the unexpanded atomic cloud with $N = 9.4\times10^4$. The patterns of SR intensity ($\propto |E_{\mathrm{SR}}(\mathbf{r},t)|^2$) at several selected times are displayed in Fig. 5b of the main text. The dependence of the decay rate γ_{bw} of the first SR burst on the atom number N can be also derived from our simulation as shown in Fig. 5c.

One may further extract the frequency shift $\Delta_{\mathrm{SR}} = \omega_{\mathrm{SR}} - \omega_0$ of the SR central frequency ω_{SR} relative to the atomic transition ω_0 from the SR spectrum $S(\omega) \propto \left|\int_{\tau_{\mathrm{p}}}^{\infty}[\iint E_{\mathrm{SR}}(\mathbf{r},t)d^2\mathbf{r}]e^{i(\omega-\omega_0)t}dt\right|^2$. The resulting $S(\omega)$ is depicted in Fig. 6a of the main text, where the spectrum peak is red shifted from the atomic resonance ω_0 by $\sim 2\pi\times 152$ kHz. However, this frequency shift also includes the offset frequency $\sim 2\pi\times 54$ kHz of the envelope varying. Consequently, the SR (carrier) frequency shift Δ_{SR} is equal to $-2\pi\times 98$ kHz, which reasonably agrees with the experimental results in Fig. 3d of the main text. The numerically-derived dependence of Δ_{SR} on the atomic density ρ is shown in Fig. 6b of the main text.

From the simulation results, one can further compute the superradiance efficiency. The total power of the pump field is given by $P_{\mathrm{p}}(t) \propto \iint \left|E_{\mathrm{p}}(\mathbf{r},t)\right|^2 d\mathbf{r}$ while the total power of the SR field output from the fibre is $P_{\mathrm{SR}}(t) \propto \iint |E_{\mathrm{SR}}(\mathbf{r},t)|^2 d\mathbf{r}$. Figure 6c of the main text shows the time-dependent $P_{\mathrm{p}}(t)$ and $P_{\mathrm{SR}}(t)$ for the unexpanded atomic cloud ($l_z = 0.87$ mm) with $N = 9.4\times10^4$. Within the π-pulse period, $P_{\mathrm{p}}(t)$ is higher than $P_{\mathrm{SR}}(t)$ and the difference $P_{\mathrm{ab}} = \int_0^{\tau_{\mathrm{p}}}\left(P_{\mathrm{p}}(t) - P_{\mathrm{SR}}(t)\right)dt$ corresponds to the energy absorbed by the atomic cloud. In contrast, $P_{\mathrm{em}} = \int_{\tau_{\mathrm{p}}}^{\infty} P_{\mathrm{SR}}(t)dt$ denotes the SR-field energy emitted by the excited atoms. We should point out that SR may start before τ_{p}. The SR efficiency κ defined in the main text is then given by

$\kappa = P_{\mathrm{em}}/P_{\mathrm{ab}}$. Figure 6d of the main text plots the dependence of κ on the atomic number N for the unexpanded cloud (i.e., $l_z = 0.87$ mm), corresponding to Fig. 4b of the main text. We see that κ goes up as N is increased and is saturated eventually. Curve fitting leads to $\kappa = \chi(\eta N)/(1+\eta N)$ with the coupling coefficient $\chi = 0.87$ and the single-atom cooperativity parameter $\eta = 3.6 \times 10^{-5}$. We find that κ presented in Fig. 6d of the main text is lower than that of Fig. 4b in the main text. This is mainly attributed to the difference between the calculated transverse fibre eigenmodes $\psi_{m=0,\ldots,8}(\mathbf{r})$ and those propagating in the real fibre. In addition, the insufficient number of the fibre modes, whose intensity profiles do not peak at the centre of the fibre core, joining in the atom-light interaction may also reduce the numerically-simulated efficiency κ.

We also calculate the fundamental-mode radiation efficiency κ_0, where the estimated coupling efficiencies for different HC-PCF eigenmodes to the single-mode fibre are: 0.60 for $|\psi_0(\mathbf{r})|^2$, 0.33 for $|\psi_5(\mathbf{r})|^2$, 0.05 for $|\psi_5(\mathbf{r})|^2$, and 0.00 for others. Figure 6d of the main text also depicts the numerical results of κ_0 corresponding to Fig. 4b of the main text.

Supplementary References

1. Okaba, S., Takano, T., Benabid, F., Bradley, T., Vincetti, L., Maizelis, Z., Yampol'skii, V., Nori, F. & Katori, H. Lamb-Dicke spectroscopy of atoms in a hollow-core photonic crystal fibre. *Nature Commun.* **5**, 4096 (2014).
2. Lehmberg, R. H. Radiation from an *N*-Atom System. I. General formalism. *Phys. Rev. A* **2**, 883-888 (1970).
3. Alharbi, M., Bradley, T., Debord, B., Fourcade-Dutin, C., Ghosh, D., Vincetti, L., Gérôme, F. & Benabid, F. Hypocycloid-shaped hollow-core photonic crystal fiber Part II: Cladding effect on confinement and bend loss. *Opt. Express* **21**, 28609-28616 (2013).

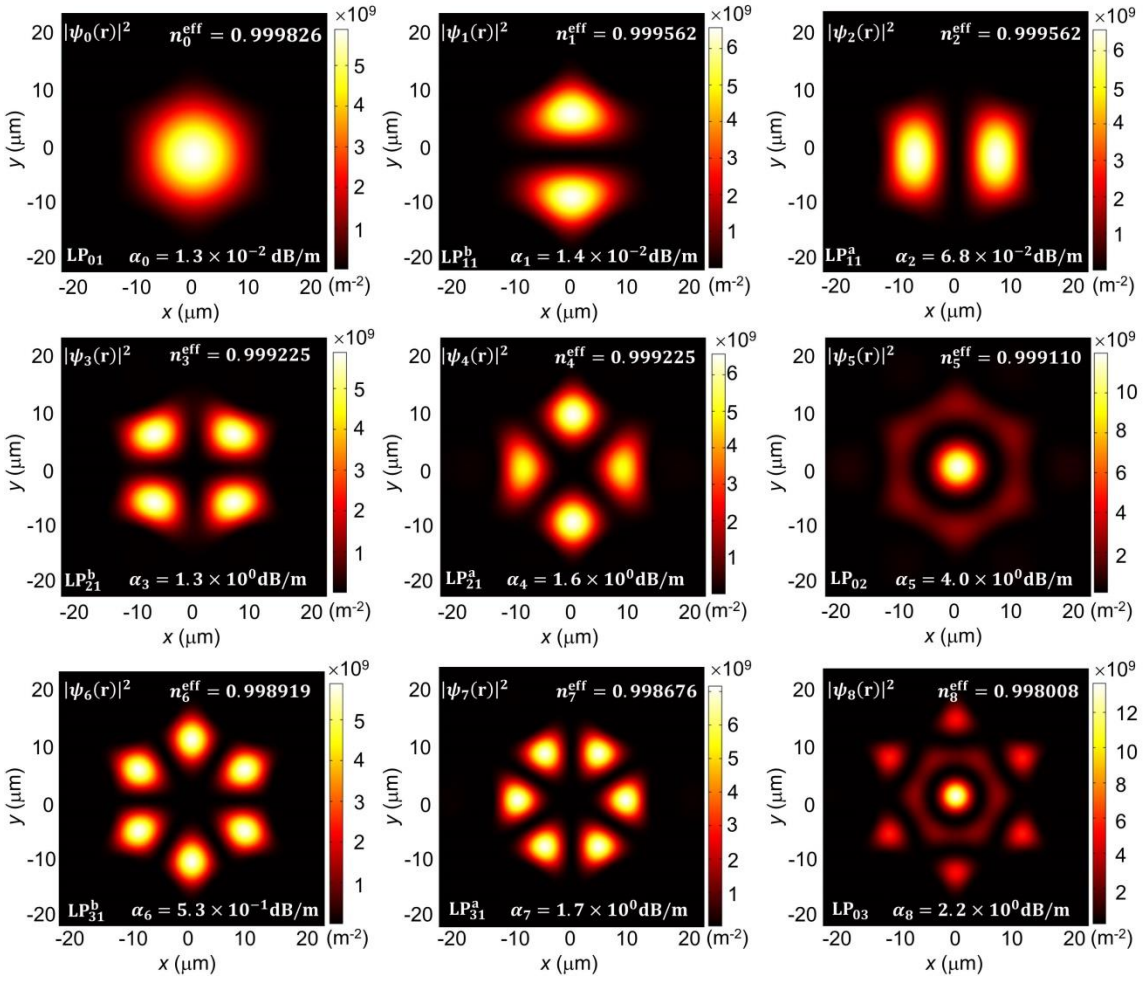

Supplementary Figure 1 | Transverse Fibre modes. Intensity distribution of different $\psi_{m=0,1,\ldots,8}(\mathbf{r})$ fibre modes and their effective refractive indices $n_{m=0,1,\ldots,8}^{\text{eff}}$ and confinement loss coefficients $\alpha_{m=0,1,\ldots,8}$ derived by using the full-vector finite element method[3]. The intensity profiles of $\psi_0(\mathbf{r})$, $\psi_5(\mathbf{r})$ and $\psi_8(\mathbf{r})$ own the central peaks while that of others minimize at the central point of fibre cross section.

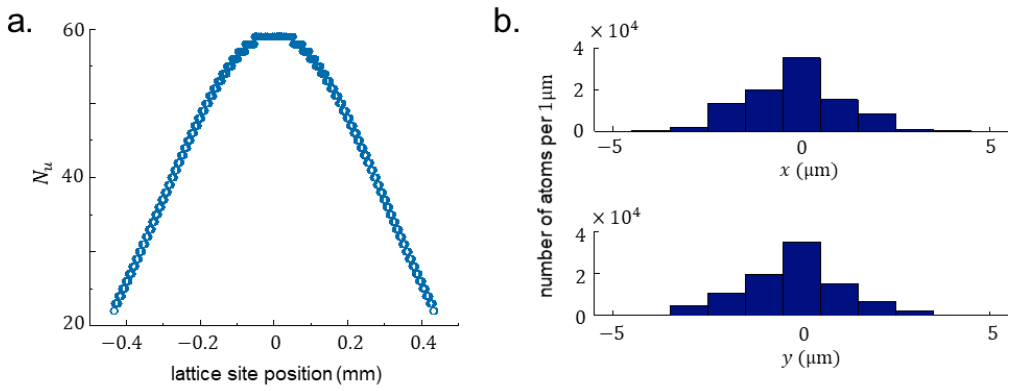

Supplementary Figure 2 | $N = 9.4 \times 10^4$ atoms inside lattice region. (a) Number N_u of atoms in different lattice sites. The characteristic width of the atomic cloud is $l_z = 0.87$ mm. (b) Histograms of atomic distributions along x- and y-directions. The characteristic radial radius of the atomic cloud is $r_\mathrm{a} = 1.7$ μm.